Summer 2014

Synthesis and characterization of crystalline iron nanoparticles from zerovalent iron sandwich complexes

Anh Tue Nguyen
Purdue University

Graduate School ETD Form 9
(Revised 12/07)

PURDUE UNIVERSITY
GRADUATE SCHOOL
Thesis/Dissertation Acceptance

This is to certify that the thesis/dissertation prepared

By Anh Tue Nguyen

Entitled SYNTHESIS AND CHARACTERIZATION OF CRYSTALLINE IRON NANOPARTICLES FROM ZEROVALENT IRON SANDWICH COMPLEXES

For the degree of Master of Science

Is approved by the final examining committee:

Alexander Wei
Chair

Scott A. McLuckey

Chengde Mao

To the best of my knowledge and as understood by the student in the *Research Integrity and Copyright Disclaimer (Graduate School Form 20)*, this thesis/dissertation adheres to the provisions of Purdue University's "Policy on Integrity in Research" and the use of copyrighted material.

Approved by Major Professor(s): Alexander Wei

Approved by: R. E. Wild 5/12/2014
Head of the Graduate Program Date

SYNTHESIS AND CHARACTERIZATION OF CRYSTALLINE IRON NANOPARTICLES FROM ZEROVALENT IRON SANDWICH COMPLEXES

A Thesis

Submitted to the Faculty

of

Purdue University

by

Anh Tue Nguyen

In partial Fulfillment of the

Requirements of the Degree

of

Master of Science

August 2014

Purdue University

West Lafayette, Indiana

ACKNOWLEDGEMENTS

First of all, I would like to thank my advisor, Professor Alexander Wei, for his guidance during the time I was studying at Purdue. I appreciate for his knowledge, support, which helped me to complete the research project and thesis writing.

I thank my committee members Professor Scott A. McLuckey, Professor Chengde Mao. I especially would like to thank Professor Chengde Mao for his help and kindness.
I would like to acknowledge Professor Alvaro Duarte Ruiz for his collaboration during the beginning of the project. I also want to thank Dr. Chris Gilpin and Laurie Muller for the training and assistance in the electron microscopy. I express my appreciation to my lab-mates for their help and kindness; especially to Naveen Reddy Kadasala, for his time and effort in collecting the XRD data for the project.

Last but not least, I want to thank my family members and my girlfriend for their love, support, and encouragements.

.

TABLE OF CONTENTS

Page

LIST OF TABLES

LIST OF FIGURES

Figure Page

ABSTRACT

Nguyen, Anh Tue. M.S., Purdue University, August 2014. Synthesis and Characterization of Crystalline Iron Nanoparticles from Zerovalent Iron Sandwich Complexes. Major Professor: Alexander Wei.

In this project we present a systematic study on the synthesis of crystalline iron nanocubes by thermal decomposition of an iron sandwich complex, (π-C_5H_5)Fe^0(π-C_6H_7), in the presence of oleylamine and oleylamine.HCl as surfactants and *n*-decane as a solvent. The presence of oleylamine.HCl is essential for the reproducible formation of crystalline iron cores.

Reaction parameters such as temperature, surfactant concentration, effect of counterion, and organoiron reagent structure were investigated in order to obtain iron nanoparticles with uniform size and shape. The nanoparticles, which were characterized by TEM, HRTEM, SAED, and XRD, were determined to have core/shell structures, with the former composed of bcc-Fe and the latter composed of iron oxide (Fe_3O_4 or Fe_2O_3).

CHAPTER 1

MAGENETISM AND MAGNETIC MATERIALS

1.1 Introduction

Magnetism is an intrinsic phenomenon to many materials that exert a repulsive or attractive force on other materials. Iron, cobalt, nickel, and iron oxides are well-known examples of materials that exhibit magnetic properties. Many modern technological devices use magnetic materials including electrical power generators and transformers, electric motors, loudspeakers, computer, hard drives and components of sound and video reproduction systems.[1]

1.2 Origins of Magnetic Moments

The magnetic properties of materials originate from two types of electronic motions: the orbital motion of electrons around the nucleus and the spin or precession of the electron about its own axis (Figure 1.1). An electron orbiting around the nucleus of an atom generates a very small magnetic field, producing a magnetic moment along its axis of rotation. The other magnetic moment originates from spin of each free electron. The net magnetic moment per atom is thus the sum of the moments from orbital and electron spin contributions.

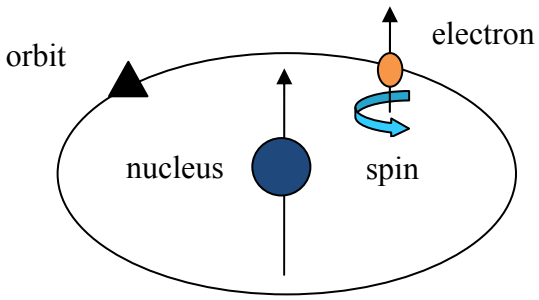

Figure 1.1 A free electron orbits around the nucleus of an atom, while spinning about its own axis.

1.3 Variables in Magnetism

The external magnetic field strength is designated as *H*. The magnetic induction, or magnetic flux density, which is denoted as *B*, is the magnitude of the field strength generated within a material that is subjected to an external field. Both *B* and *H* are field vectors, and are related as:

$$B = \mu H \qquad (1.1)$$

where μ is the relative permeability, a property of the specific medium through which the *H* field passes and in which *B* is measured. In a vacuum,

$$B_o = \mu_o H \qquad (1.2)$$

where μ_o is the permeability in vacuum, which has a value of $4\pi \times 10^{-7}$ (H/m).

The magnetization term, *M*, is defined as the quantity of magnetic moment per unit volume. The relationship between *B*, *H* and *M* is expressed as:

$$B = \mu_o(M + H) \qquad (1.3)$$

The magnitude of *M* is proportional to the applied field as follows:

$$M = \chi_m H \qquad (1.4)$$

where χ_m is the magnetic susceptibility, a dimensionless constant that describes the degree of magnetization of a material when subjected to an external magnetic field.

1.4 Magnetism of Materials

The magnetic properties of materials can be classified based on how they respond to external magnetic fields. The main categories are diamagnetism, paramagnetism and ferromagnetism; the latter also includes ferrimagnetism and antiferromagnetism, which are temperature-dependent subclasses of ferromagnetism.[1]

1.4.1 Diamagnetism

Diamagnetic substances are composed of atoms which have no net magnetic moments (i.e., there are no unpaired electrons). When exposed to a field *H*, a weak magnetization is produced in a direction opposite that of the applied field. (Figure 1.2)

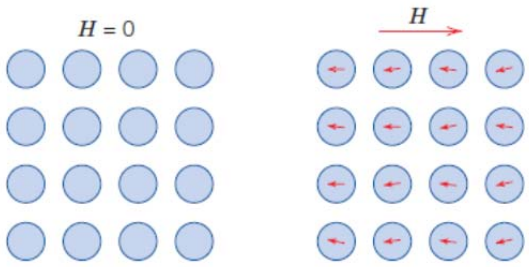

Figure 1.2 The magnetic state of a diamagnetic material, with and without a magnetic field.[1]

1.4.2 Paramagnetism

In this class of materials, some atoms have unpaired electrons that can give rise to a net magnetic moment, but the net magnetization of materials returns to zero when the field is removed. In the presence of a magnetic field, there is a partial alignment of the magnetic moments in the field direction (Figure 1.3).

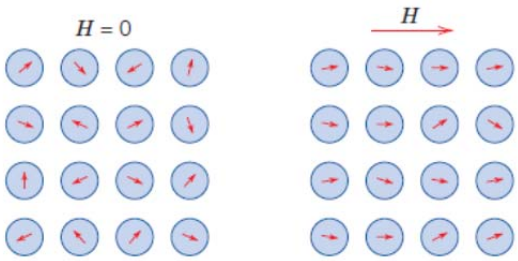

Figure 1.3 Magnetic state of a paramagnetic material, with and without an external magnetic field.[1]

1.4.3 Ferromagnetism

Ferromagnetic materials exhibit a net alignment of spins resulting in a non-zero magnetization even in the absence of a magnetic field (Figure 1.4). The elements Fe, Ni, and Co and many of their alloys are typical ferromagnetic materials.

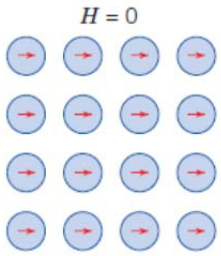

Figure 1.4 Spontaneous alignment of atomic moments in a ferromagnetic material, in the absence of an external magnetic field (H=0).[1]

1.4.4 Ferrimagnetism

In a ferromagnetic material, the magnetic moments in different sublattices are of varying strength and typically oppose each other, resulting in a partial cancellation. However, the opposing moments are unequal and result in a net magnetization (Figure 1.5). This is commonly observed in ferrites whose sublattices consist of different atoms or species (e.g. Fe^{2+} and Fe^{3+}).

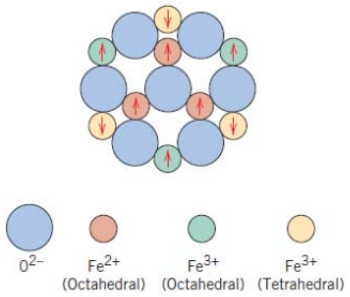

Figure 1.5 The spin magnetic moment configuration for Fe^{2+} and Fe^{3+} ions in Fe_3O_4.[1]

1.4.5 Antiferromagnetism

Like ferrimagnetism, the magnetic moments can be assigned to anti-parallel sublattices, A and B. If these moments are exactly equal and opposite, the net moment is zero. This type of magnetic ordering is called antiferromagnetism.

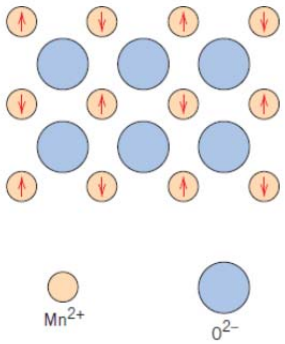

Figure 1.6 Anti-parallel alignment of magnetic moments in antiferromagnetic manganese oxide.[1]

1.5 Some Important Concepts for Ferromagnetic and Ferrimagnetic Materials

The influence of temperature on magnetic behavior: At sufficiently high temperature, the atomic thermal motions overcome the coupling interactions between adjacent atomic moments. The result is a decrease in the saturation magnetization of materials. This critical temperature is denoted as T_c, or Curie temperature. The saturation magnetization is at maximum at 0 K, at which thermal vibrations are at a minimum. With increasing temperature, the saturation magnetization decreases gradually, and sharply drops to zero at T_c. Both ferromagnetic and ferrimagnetic materials are paramagnetic above the Curie temperature. The magnitude of T_c varies with material; for example, the respective T_c values for iron, cobalt, nickel, and Fe_3O_4 are 768, 1120, 335, and 585 ^oC.[1]

Magnetic Domains: Ferromagnetic and ferrimagnetic materials at temperatures below T_c are composed of many domains, in which domain the magnetic spins align with one another and form a net moment. The magnetized domains are separated by domain walls, across which the directions of magnetization abruptly change. The bulk magnetization for a material is the sum of magnetizations from all the domains.

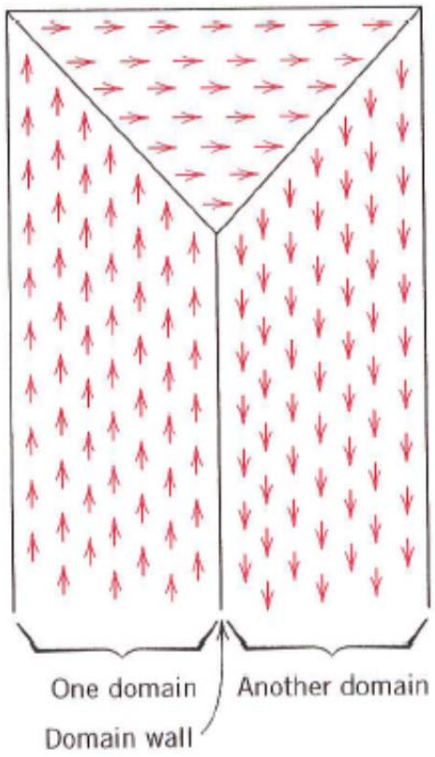

Figure 1.7 Illustration of domains in ferromagnetic or ferrimagnetic materials; arrows represent atomic magnetic dipoles. Within each domain, all dipoles are aligned, whereas the direction of alignment varies from one domain to another.[1]

Hysteresis: When an external magnetic field is applied to a ferrimagnet with initially zero moment, the magnetic moments align themselves with it. They will often remain aligned even after the field is removed (H=0). This behavior is called hysteresis

and a plot of magnetization M with magnetic field H is called a hysteresis loop. The hysteresis loop is a common feature when characterizing magnetic materials, and various parameters can be determined from it (Figure 1.8).

The magnetization M increases with external field H, and reaches a maximum value called the saturation magnetization (M_s). When H is reduced from the saturation point, the curve does not retrace its original path, producing a hysteresis effect in which M lags behind H. At H=0, a remanent magnetization M_r indicates the extent to which spins remain aligned, even in the absence of external field H. Applying a field in the reverse direction brings the magnetization M back to zero at a threshold called the coercive field, H_c. Saturation magnetization will be eventually achieved in the negative direction when the reversed field H is sufficiently high. If the external field is then applied again in the positive direction, the full hysteresis loop can be plotted. The area contained within the loop indicates the amount of energy absorbed by the material during each cycle of the hysteresis loop.

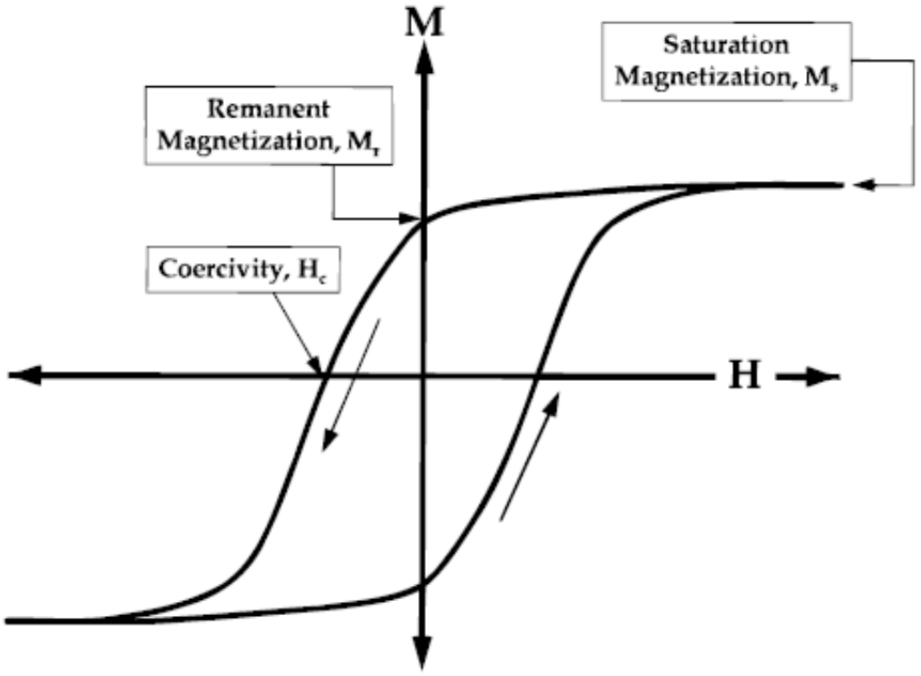

Figure 1.8 Hysteresis loop (magnetization vs. field).[2]

MRI (Magnetic Resonance Imaging): MRI Contrast agents currently in use involve paramagnetic ions, specifically gadolinium which has a very high moment for a paramagnetic species, but still well below what is achievable in superparamagnetic materials. Superparamagnetic iron oxides have been commercialized as MRI contrast agents, and offer a number of advantages beyond their magnetic relaxation.[3]

Iron nanoparticles could also be used as a contrast agent, and may provide a much improved MRI contrast when compared with iron oxide nanoparticles.[4] The clear advantage of metallic iron is that its saturation magnetization is roughly double that of Fe_3O_4. The disadvantage is that metallic iron is not stable under biological conditions, and would require a coating to prevent oxidation and loss of magnetism.

Magnetic hyperthermia*:* Hyperthermia is a medical treatment that relies upon locally heating tissue above 42^{o}C to destroy diseased tissues, particularly tumors. Godon and co-workers used submicron iron particles for hyperthermia treatment in 1979,[5] with inductive heating using a high-frequency AC field. The field energy is converted to heat through hysteresis losses and the resistive dissipation of eddy currents. An ideal material for magnetic hyperthermia would have a high M_s value and low anisotropy, which, of course, describes the magnetic properties of iron perfectly.

1.6 Magnetic Properties of Nanoparticles

In the case of bulk materials, their magnetic properties (e.g., saturation magnetization M_s, coercive field H_c, and Curie temperature T_c) are independent of the size or shape of samples.[6] However, magnetic properties of nanoparticles are strongly influenced by size and also by surface phenomena. For example, many magnetic nanoparticles exhibit superparamagnetism at room temperature, a phenomenon not observed in bulk magnetic materials.

In bulk ferromagnetic materials, the spins of unpaired electrons are spontaneously aligned with those of magnetic neighboring atoms. To decrease the overall energy of the system, the material breaks into multiple magnetic domains to limit the leakage of magnetic flux. However, there is also an energy cost for domain wall formation. Therefore, when the size of the ferromagnetic particles has decreased to a critical diameter, the formation of domain walls becomes energetically less favorable and the particles exhibit a single domain with a net moment. In other words, a magnetic particle

maintains a single domain if the energy required to create a domain wall is greater than the energy cost of magnetic flux loss.

Magnetization reversal in single-domain nanoparticles occurs via spin rotation since there are no domain walls to move. Because of this, single-domain particles have a larger coercivity compared to multi-domain systems as it takes more energy to rotate the magnetization than to move a domain wall.

In the absence of an external magnetic field, the magnetic moment of a single-domain nanoparticle can randomly flip direction under the influence of thermal energy. The typical time between two switches in magnetic moment direction is called the *Néel relaxation time*, t_N. When the time used to measure the magnetization t_m of the nanoparticles is much longer than the t_N, the average magnetization appears to be zero, and the nanoparticles are considered to be in the superparamagnetic state. If $t_m << t_N$ then the nanoparticles exhibit remanent magnetization. The threshold temperature between these two states is called the blocking temperature, or t_B.

There are two important reasons why the magnetic properties of superparamagnetic particles are so useful. First, the magnetic moments can reorient under relatively low fields, meaning that superparamagnetic particles can have very high initial susceptibilities. Another useful property of superparamagnetic nanoparticles is that they have no coercivity. When the field is removed, thermal energy allows superparamagnetic nanoparticles to freely reorient their magnetic moments so that no external field is needed to demagnetize them.[3]

1.7 Synthesis and Application of Iron Nanoparticles

The synthesis of stable magnetic nanoparticles with a high saturation magnetization has been a goal in biomedical imaging, sensing and therapeutic applications. Among the transition-metal elements, Fe is the most abundant and has a high saturation magnetization (σ_s) at room temperature (218 A m^2 kg^{-1}).[3] Probably the greatest limitation of iron is its sensitivity to water and oxygen. Iron nanoparticles smaller than 8 nm will be completely oxidized to Fe_2O_3 or Fe_3O_4 upon exposure to air.[4b] The difficulty in maintaining iron nanoparticles in their zero-valent state restricts their use to situations where water and oxygen are largely excluded. Controlling the oxidation of iron nanoparticles is one strategy to limit their corrosion: a stable oxide shell can allow the nanoparticles to be handled in air or water at least for limited periods of time.

Fe nanoparticles (NPs) are commonly synthesized by the thermal decomposition of iron pentacarbonyl, $Fe(CO)_5$.[7] For example, amorphous iron nanoparticles are produced by sonolysis of $Fe(CO)_5$ in the presence of polyvinylpyrrolidone or oleic acid.[6b, 7] Hyeon and co-workers have described the synthesis of *bcc*-Fe particles including nanorods although their magnetization was not reported.[9] More recently, Sun and co-workers have developed an approach that leads to single-crystalline 15 nm bcc-FeNPs.[4a] Once exposed to air these FeNPs are only partially oxidized, resulting in core/shell bcc-Fe/Fe_3O_4 NPs with a 10 nm bcc-Fe core are stable in air and have a high magnetization value (164 A.m^2.kg^{-1}).

Additional reports include the use of other precursors, e.g. the reductive decomposition of bis(amido)iron(II) complexes Fe_2[10] and iron(III) acetylacetonate ($Fe(acac)_3$),[11] which can produce cubic Fe NPs with excellent size control. However, all

of these processes are limited in terms of ease of synthesis and scalability: $Fe(CO)_5$ is volatile and highly toxic,[3] and other processes involve precursors that are expensive and air-sensitive,[10,12] or require high decomposition temperatures.[11]

Recently, Tilley and coworkers used an air stable iron sandwich complex, $Fe(C_5H_5)(C_6H_7)$, as the precursor for single-crystal iron NPs under solvothermal conditions.[4b] The iron NPs were synthesized by thermal decomposition of $Fe(C_5H_5)(C_6H_7)$ in the presence of oleylamine at 130 ^oC under a hydrogen atmosphere. The as-synthesized FeNPs were exposed to air, generating highly crystalline iron/iron oxide core/shell NPs. Once the surfactant oleylamine was replaced by dimercaptosuccinic acid (DMSA), the DMSA-coated NPs could be dispersed in water and were stable for at least six months.

Figure 1.9a shows a TEM image of the synthesized core/shell NPs with an average particle size of 16 ± 1.5 nm. The contrast of the NPs shows a darker core and lighter shell suggests the formation of core/shell structures. In HR-TEM image (Figure 1.9b), spacing corresponding to α-Fe (110) were observed in the core and spacing matching iron oxide were observed on the shell. The XRD pattern (Figure 1.9c) also indicates the presence of α-Fe and iron oxide. Figure 1.9d indicates the magnetization saturation value of the iron/iron oxide core/shell NPs is 150 emu g^{-1} at 6 T.

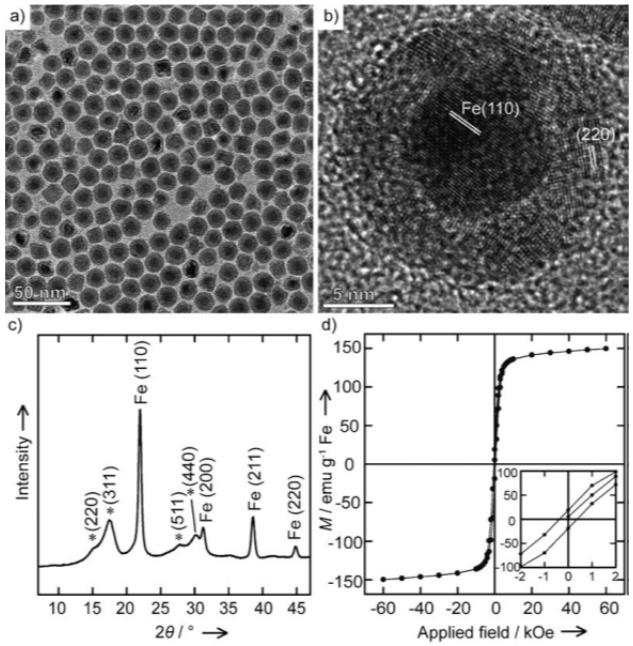

Figure 1.9. a) TEM image of iron/iron oxide core/shell nanoparticles. b) HRTEM image showing a core/shell structures. c) XRD pattern of the nanoparticles obtained using synchrotron radiation (λ=0.775 A^{o}). d) Magnetization (M) of the core/shell nanoparticles at 300 K, with inset showing the low-field region.[4b]

CHAPTER 2

SYNTHESIS AND CHARACTERIZATION OF IRON NANOPARTICLES

2.1 Experimental Studies

2.1.1 Synthesis of Iron Nanoparticle Precursor (π-C_5H_5)Fe^0(π-C_6H_7) (CpFe(benz-H))

The synthesis of CpFe(benz-H) was performed according to a previously described method (Scheme 2.1).[13] Typically, ferrocene (10 g) was refluxed in benzene (65 mL) with $AlCl_3$ (3 eq.), Al (1 eq., cleaned with 6 M HCl) and a few drops of water for 1.5 hours, then poured over ice. The aqueous phase was separated and washed with hexanes three times. The aqueous solution was treated with addition of KPF_6 (1.23 equiv.), which caused the precipitation of a green solid. This was filtered and dried under vacuum to produce 15 g of CpFe(benzene)-PF_6 salt (80% yield). The green solid was filtered and dried under vacuum for the next step.

The CpFe(benzene)-PF_6 salt was suspended in dry THF and cooled in an ice bath, then treated with $LiAlH_4$ (2.5 equiv) in portions. After 15 min, the reaction was quenched with water. The orange/red reaction mixture was transferred to a separatory funnel, diluted with H_2O, and extracted 3 times with hexanes. The hexane fractions were dried over $NaSO_4$, filtered and concentrated to give a red solid, which was purified by

sublimation at 65 ^{o}C and 0.5 torr (Figure 2.1). The isolated yield of CpFe(Benz-H) was 5.8 g (65% yield).

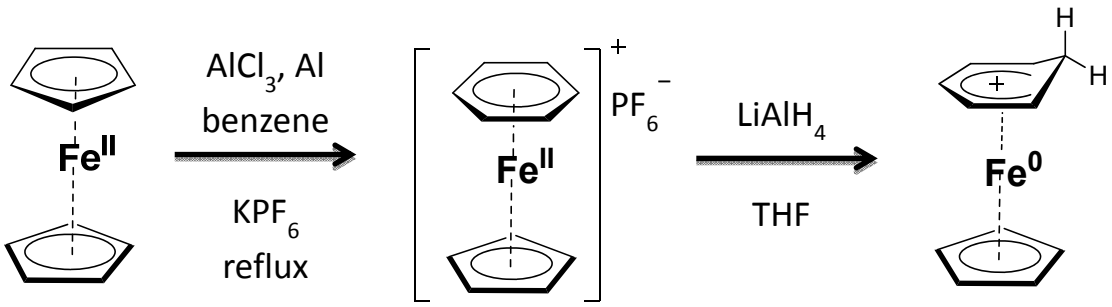

Scheme 2.1. Synthesis of iron nanoparticle precursor (π-C_5H_5)Fe^0(π-C_6H_7).

Figure 2.1 (π-C_5H_5)Fe^0(π-C_6H_7) CpFe(benz-H) after sublimation.

2.1.2 Synthesis of Oleylamine.HCl

1 mL of oleylamine was heated at 50−60 ^{o}C under reduced pressure (aspirator) to decompose residual carbamate and to remove adventitious CO_2, then dissolved at room temperature in 10 mL heptanes, and cooled to 0 ^{o}C in an ice bath. HCl gas was freshly generated in a separate two-neck round-bottomed flask containing 5.5 g of NaCl (101 mmol), which was treated dropwise with 2.6 mL of concentrated H_2SO_4 (93.2 mmol) with vigorous magnetic stirring. HCl gas was bubbled into the reaction flask with oleylamine using positive pressure from an argon balloon. The reaction mixture was

cooled to −20 ^{o}C to produce a white precipitate, then centrifuged for 10 minutes at 5000 rpm. The supernatant was discarded, and the oleylamine.HCl was dried under vacuum.

2.1.3 Synthesis of Iron Nanoparticles from (π-C_5H_5)Fe^0(π-C_6H_7)

All solvothermal reactions were carried out in thick-walled glass reaction vessels. In a typical experiment, the vessel was flame-dried to remove moisture prior to adding CpFe(benz-H) (150 mg, 250 mM) and oleylamine.HCl (OAm.HCl) (22.8 mg, 25 mM). The reaction vessel was flushed 3 times with vacuum and argon, then treated with oleylamine (OAm) (740 µL, 750 mM) and solvent (3 mL) , then flushed with argon for 1 hour. The reaction vessel was sealed placed in an oil bath pre-heated to 130 ^{o}C for 48 hours (Scheme 2.2). The iron nanoparticles were collected by magnetic precipitation at room temperature, resuspended in hexanes and precipitated again, then washed 3 times with 2 mL of absolute ethanol, before drying under vacuum. The dry weight of the final product was 20 mg (50% yield based on Fe).

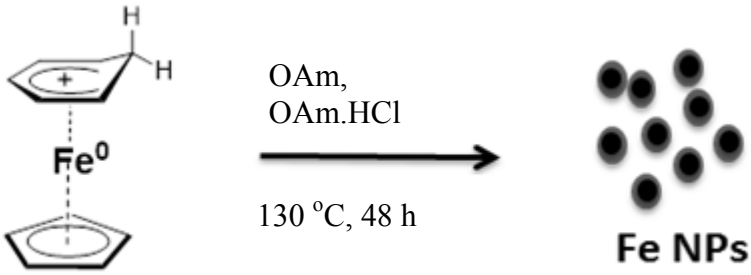

Scheme 2.2 Synthesis of Fe nanoparticles from iron precursor CpFe(benz-H).

2.2 Characterization Methods

Fe NPs were characterized by standard and high-resolution transmission electron microscopy (HR-TEM), selected area electron diffraction (SAED), and powder X-ray diffraction (XRD). Magnetic properties were measured using a superconducting quantum interference device (SQUID) magnetometer, in collaboration with Dr. Xiao-Min Lin (Argonne National Laboratory).

2.2.1 Transmission Electron Microscopy (TEM)

An electron microscope with a field-emission gun (FEI Tecnai G2 20) was used to characterize nanoparticle size, shape, and crystal lattice structures at an acceleration voltage of 200 kV. 400-mesh carbon coated copper grids (Electron Microscopy Sciences) were used to prepare the TEM samples. A drop of the Fe NP dispersion in hexanes was deposited onto the TEM grid and allowed to dry in air.

Selected area electron diffraction was carried out using a camera length of 175 mm (19.5 kx magnification). An evaporated aluminum thin film (Ted Pella) was used as a calibration standard.

2.2.2 X-ray Diffraction (XRD)

XRD measurements were performed using a Panalytical X'Pert Pro diffractometer with a Cu x-ray source. A 30 mg powder sample of Fe nanoparticles (prepared described above) was immobilized using double sided-tape against a copper plate, which was mounted vertically within the sample holder.

2.3 Results and Discussion

The aim of this project is to synthesize crystalline iron nanoparticles under mild reaction conditions in an inert atmosphere. The work is inspired by the report of Tilley et al.,[4b] with a systematic evaluation of various experimental parameters on the reaction outcome. In particular, we found that addition of OAm.HCl and use of *n*-decane as a solvent provided a practical and reproducible route to synthesize cubic bcc-Fe nanocrystals. The size and the shape of the iron nanocrystals were influenced by choice of solvent, variations in reaction temperature, surfactant concentration and choice of starting material. The effect of the halide counter ion (Cl^- vs Br^-) was also investigated.

2.3.1 Effect of Ionic Surfactants

Initial attempts to reproduce the published results in high-pressure reaction vessels in mesitylene under a hydrogen or argon atmosphere with OAm as the surfactant (0.25 or 0.75 M) did not produce core/shell nanoparticles, but resulted only in iron oxide as determined by HRTEM analysis (Fe_3O_4 or γ-Fe_2O_3). Adding ionic surfactants such as cetyltrimethyl ammonium bromide (CTAB) or tetraoctyl ammonium bromide (TOAB) produced some core/shell nanoparticles suggestive of Fe cores, but shape uniformity was poor, and the population of iron oxide nanoparticles remained high (Figure 2.2). This suggested that the iron cores were unstable, and oxidized readily to Fe_3O_4 or γ-Fe_2O_3.

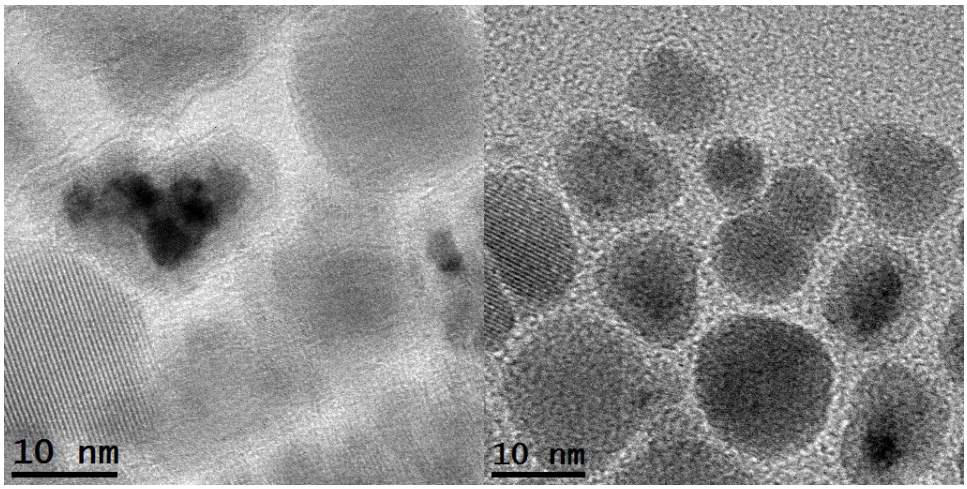

Figure 2.2 Nanoparticles synthesized by using TOAB (left) and CTAB (right) in mesitylene.

Inspired by a report by Sun et al.[4a] that the addition of HDA.HCl can produce crystalline Fe nanoparticles from iron pentacarbonyl ($Fe(CO)_5$), we attempted to decompose CpFe(benz-H) HDA.HCl in 1-octadecene containing (0.75 M OAm and 0.025 M HDA.HCl). The TEM image showed that a high population of core/shell nanoparticles was produced, and FFT analysis indicated a bcc-Fe core (Figure 2.3).

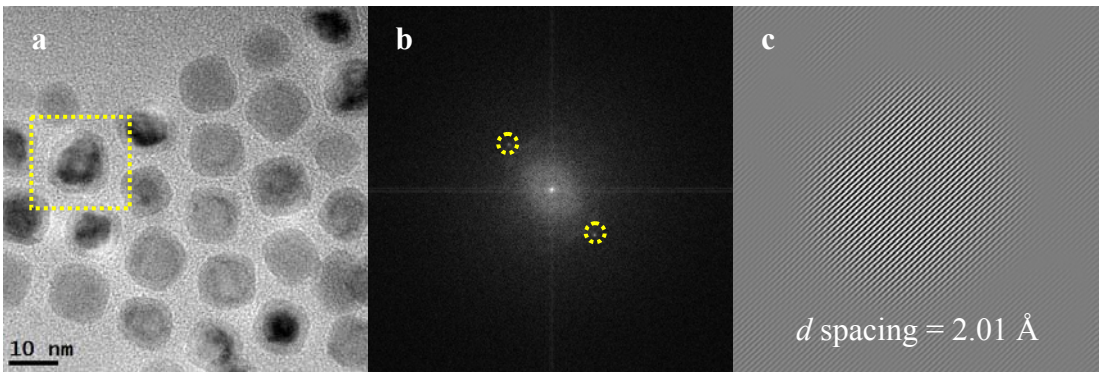

Figure 2.3 (a) TEM image, (b) FFT analysis, and (c) inverse FFT image of core/shell Fe/oxide nanoparticles prepared at 130 ^{o}C with the addition of HDA.HCl (0.025 M) in 1-octadecene.

We also determined that the addition of OAm.HCl produced cubic bcc-Fe nanoparticles with reproducible size and shape, using *n*-decane as a solvent (see Figure 2.8 and 2.11 in later sections). This means that uniform bcc-Fe nanocubes could be prepared by simply adding HCl into the reaction containing OAm.

To determine the significance of the halide counterion on nanoparticles formation, we also investigated the composition of CpFe(benz-H) (0.25 M) at 150 ^{o}C in the presence of OAm.HBr and OAm (0.025 M and 0.75 M, respectively). TEM analysis again indicated core/shell nanoparticles, but also revealed that their shapes were not cubic (Figure 2.4 and 2.5). The average size of the nanoparticles was 14.4±1.6 nm (*N*=126), slightly larger than that of the core/shell nanoparticles prepared using OAm.HCl. The addition of OAm.HCl thus became an important parameter in our nanoparticle synthesis conditions.

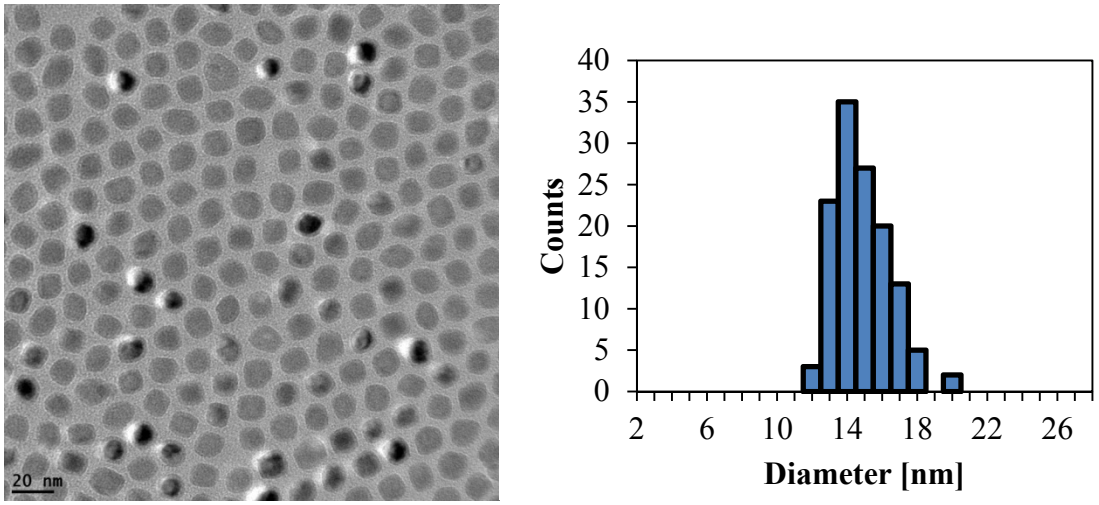

Figure 2.4 Left, TEM image of nanoparticles synthesized using OAm.HBr; right, particle size distribution (14.4 ± 1.6 nm, *N*=126).

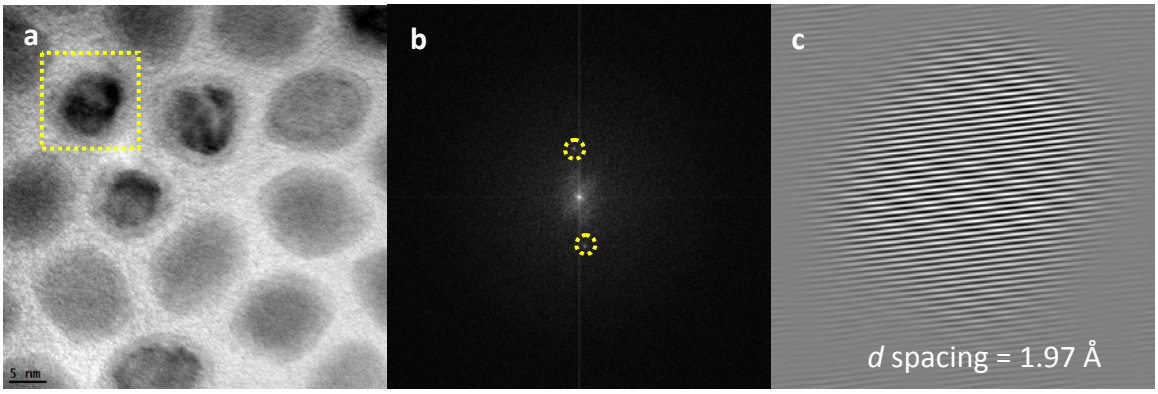

Figure 2.5 (a−c) HRTEM, FFT and inverse FFT images of a single nanoparticle from samples prepared using OAm.HBr as a co-surfactant.

2.3.2 Effect of Reaction Solvent

In a typical reaction, iron nanoparticle precursor CpFe(benz-H) (150 mg, 250 mM), oleylamine (OAm) (740 µL, 750 mM), and oleylamine.HCl (OAm.HCl) (22.8 mg, 25 mM) or hexadexylamine.HCl (HDA.HCl) (20.8 mg, 25 mM) were heated for 48 hours at 130 ^{o}C in a pre-heated oil bath using different solvents (3 mL): 1-octadecene (ODE), mesitylene, decalin and *n*-decane.

TEM images of the nanoparticles prepared in ODE were cubic and exhibited core/shell structures with an average size of 11 nm, and FFT analysis revealed bcc-Fe in the core (Figure 2.6, *left*). However, CpFe(benz-H) was poorly soluble in ODE and sublimed on the walls of the reaction vessel during the reaction, which decreased the yield of the Fe nanoparticles. Using mesitylene as solvent did not induce sublimation of CpFe(Benz-H), however the nanoparticles were irregular shape (Figure 2.6, *right*). This may be due to the propensity of mesitylene to coordinate with zerovalent Fe intermediates formed during nanoparticle growth. We thus decided to avoid using aromatic solvents in the solvothermal decomposition of CpFe(Benz-H).

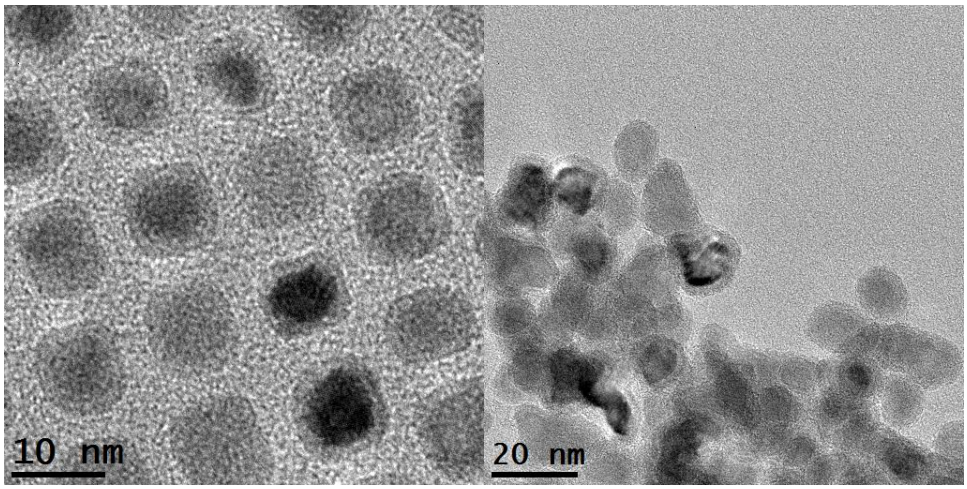

Figure 2.6 TEM images of nanoparticles synthesized using OAm.HCl (25 mM) in ODE (left) or HDA.HCl (25 mM) in mesitylene (right).

When decalin or *n*-decane were used as reaction solvent , there was no sublimation of CpFe(benz-H), and the Fe nanoparticles were uniform in size and shape (Figure 2.7). However, decalin did not provide reproducible results nanoparticles formations whereas *n*-decane consistently formed Fe nanoparticles. We thus decided to rely on *n*-decane as the solvent for synthesizing Fe nanoparticles.

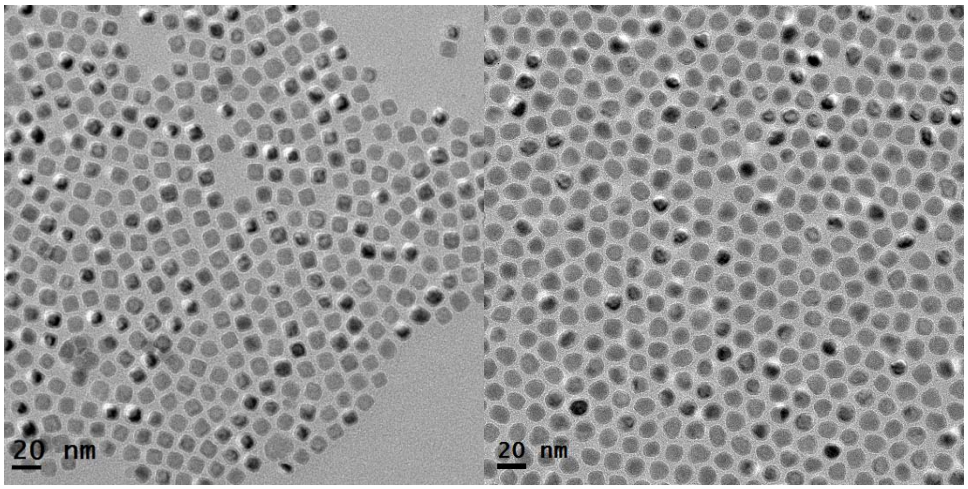

Figure 2.7 TEM images of Fe nanoparticles synthesized using OAm.HCl (25 mM) in decalin (left) or *n*-decane (right).

2.3.3 Effect of Reaction Temperature

In a typical reaction, iron nanoparticle precursor CpFe(benz-H) (150 mg, 250 mM) and oleylamine.HCl (OAm.HCl) (22.8 mg, 25 mM) were dissolved in *n*-decane (3 mL) and oleylamine (OAm) (740 μL, 750 mM). The reactions were heated for 48 hours at temperatures of 130 ^{o}C, 150 ^{o}C and 170 ^{o}C in a pre-heated oil bath, then cooled to room temperature and exposed to air during particle collection.

The TEM image of Fe nanoparticles prepared at 130 ^{o}C indicated that most of these particles were cubic. These Fe nanocubes had dark cores and surrounded by lighter shells, consistent with an iron core coated with iron oxide. The average width of the NPs in this sample was 11.8 ± 0.8 nm (*N*=148), and the average size of the Fe cores was 8.7 ± 0.8 nm (*N*=110) (Figure 2.8).

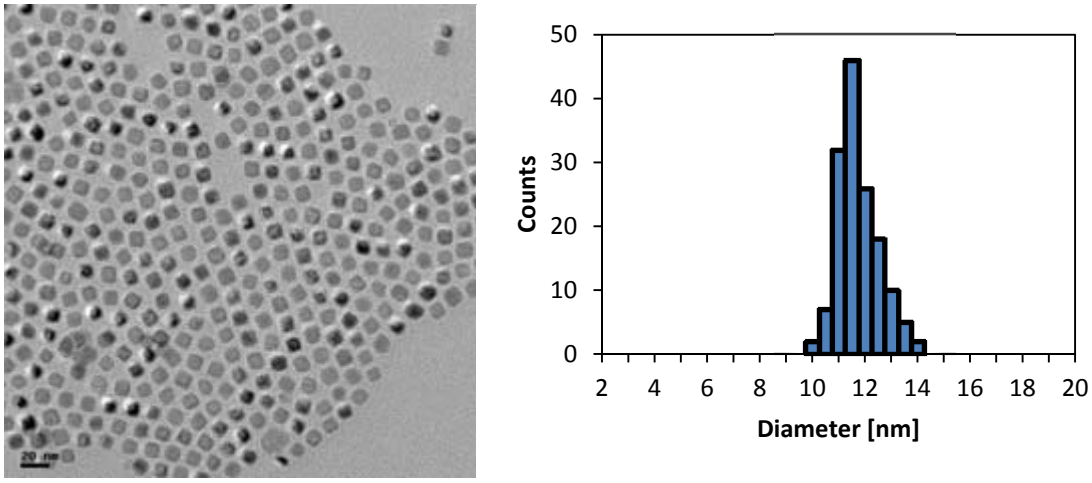

Figure 2.8 Left, TEM image of Fe nanoparticles obtained at 130 ^{o}C in *n*-decane, in the presence of OAm.HCl; right, particle size distribution (11.8 ± 0.8 nm, *N*=148).

Structural and compositional information of the nanocubes was obtained using HRTEM image analysis. A representative image of core/shell nanocubes is shown in Figure 2.9, which revealed lattice fringes in both the core and shell domains.

FFT analysis of a single nanocube (inset, dashed square) revealed several well-defined reciprocal lattice peaks (Figure 2.9). Inverse FFT analysis of bcc-Fe lattices peaks #1 and #2 coincided with the core region of the nanocube, whereas that of lattice peaks #3−#7 indicated formation of crystalline iron oxide in the shell region (Figure 2.10). The d-spacing values for bcc-Fe and iron oxide (Fe_3O_4 or γ-Fe_2O_3) are summarized in Table 2.1.

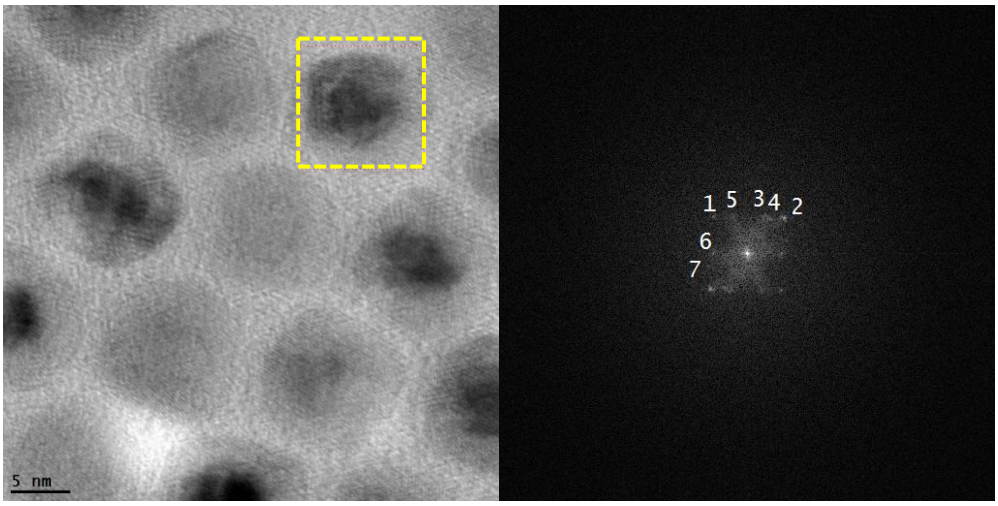

Figure 2.9 Left, HRTEM image of Fe nanocubes prepared at 130 ^{o}C; right, FFT analysis of the nanocube outlined in dashed square.

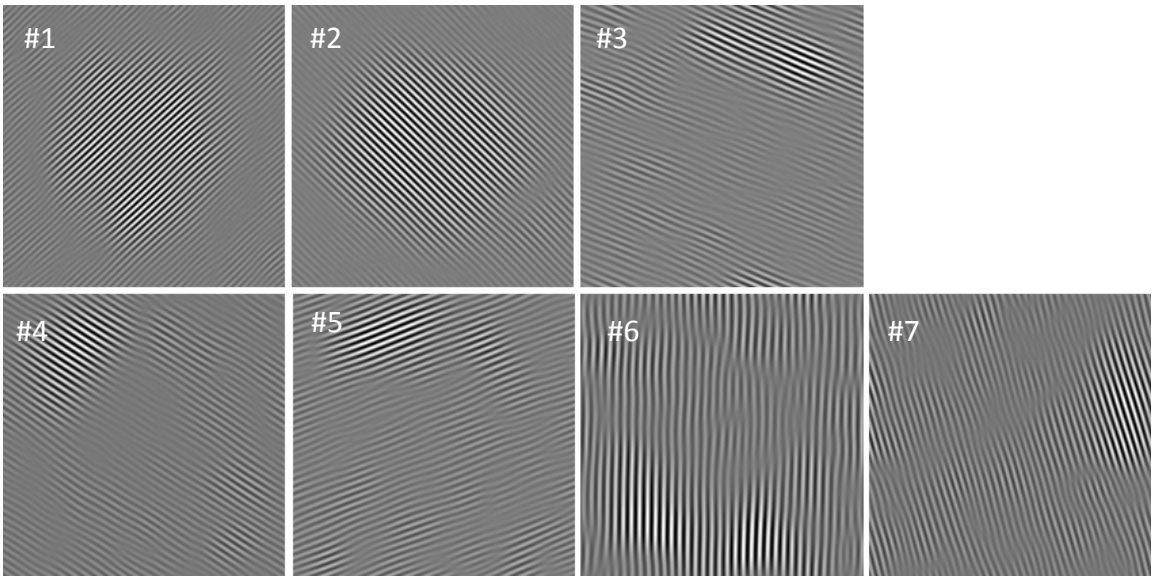

Figure 2.10 Inverse FFT analysis of the seven lattice peaks identified Figure 2.9.

Table 2.1 Lattice analysis of core/shell nanoparticles based on FFT image in Figure 2.10.

Lattice Peak #	Measured d spacing (Å)	d values (Å) JCPDS #6-0696 (bcc-Fe)	*hkl* (%)	d values (Å) JCPDS #19-0629 (Fe_3O_4)	*hkl* (%)
1, 2	2.02, 1.95	2.026	110 (100)		
3, 4, 5, 7	2.54, 2.45, 2.59, 2.53			2.53	311 (100)
6	2.98			2.97	220 (30)

When the reaction temperature was increased from 130 to 150 or 170 ^{o}C, the average NP size increased by 10 or 20%, respectively. However, the NP shapes were also affected: Fe NPs prepared at 150 ^{o}C and especially at 170 ^{o}C were less isotropic and had fewer nanocubes than those prepared at 130 ^{o}C (Figure 2.11). The effect of reaction temperature on nanoparticle size is summarized in Table 2.2.

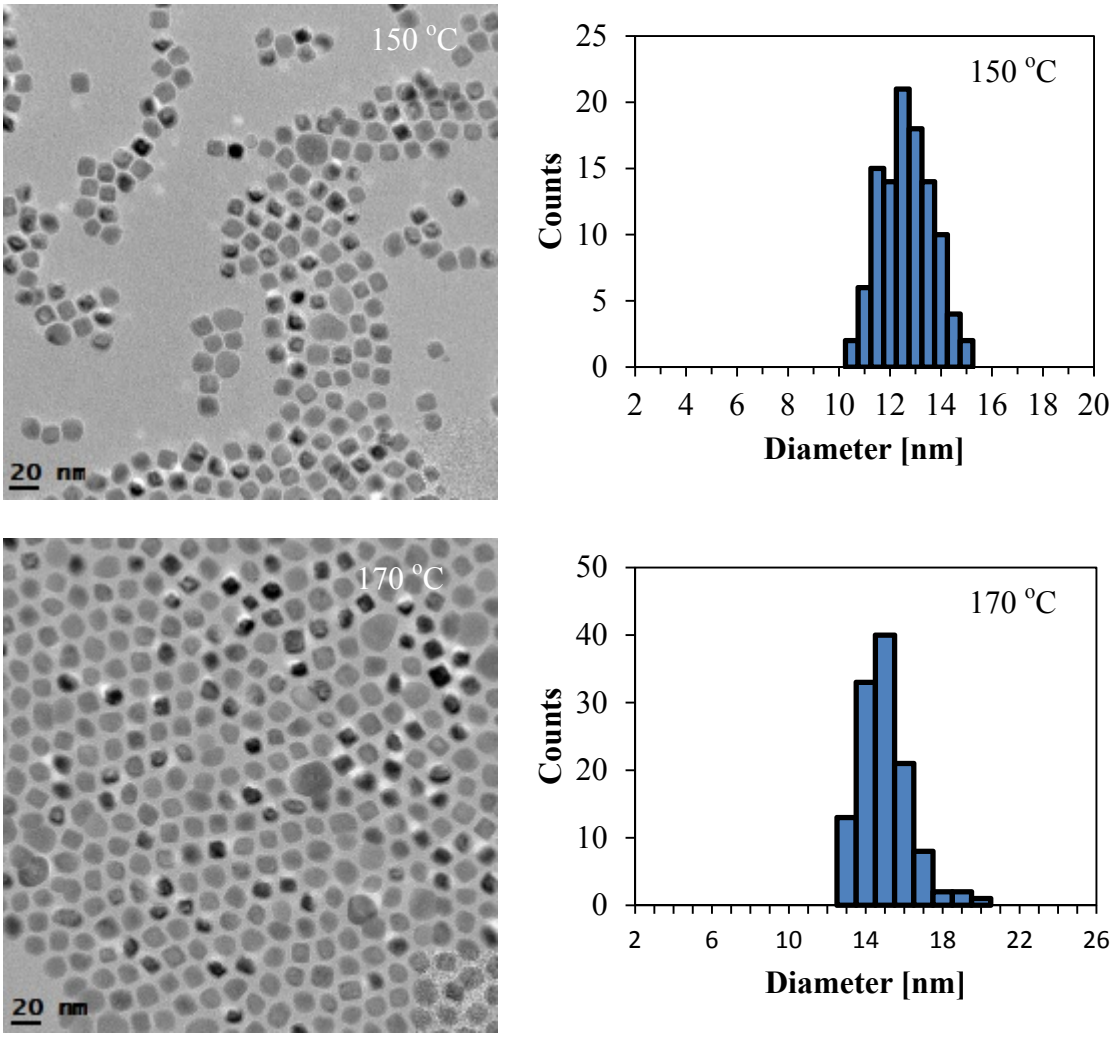

Figure 2.11 TEM images and size distribution analysis of Fe nanoparticles synthesized at 150 and 170 °C.

Table 2.2 Size of Fe nanoparticles prepared in 0.75 M OAm/25 mM OAm.HCl at different temperatures.

Reaction temperature (^{o}C)	Particle diameter (nm)	Rel. Std. Dev. (%)
130	11.8 ± 0.8 (N=148)	6.8
150	12.4 ± 1.0 (N=105)	8.1
170	14.4 ± 1.3 (N=120)	9.0

HRTEM analysis of Fe nanoparticles synthesized at 150 and 170 ^{o}C clearly revealed core/shell morphologies (Figure 2.12). Again, FFT analysis of a single nanoparticle confirmed the presence of bcc-Fe core for each sample.

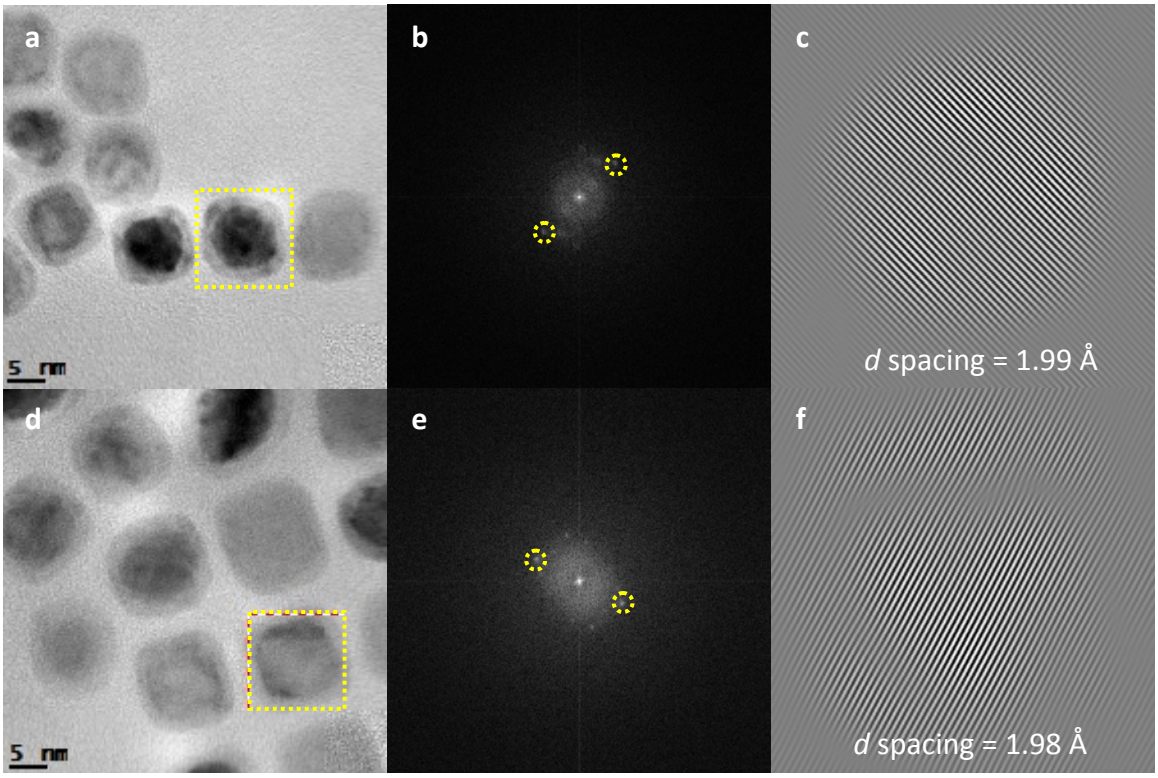

Figure 2.12 HRTEM, FFT and inverse FFT images of a single Fe nanoparticle from samples prepared at 150 ^{o}C (a−c) and 170 ^{o}C (d−f).

2.3.4 Effect of Surfactant Concentration

In this series of experiments, the concentration of CpFe(benz-H) was kept constant at 0.25 M (150 mg in 3 mL) while the surfactants OAm and OAm.HCl were scaled down by factors of 3 (0.25 M and 8.3 mM, respectively). Fe nanoparticles were again prepared by heating at three different temperatures (130, 150 and 170 ^{o}C) for 48 h.

Decreasing the ratio of surfactant to CpFe(benz-H), caused an overall increase in nanoparticle size, although it did not exhibit any clear trend with reaction temperature. The average diameter of nanoparticles synthesized at 130 ^{o}C increased from 11.8 to 15.3 nm, whereas those prepared at 150 ^{o}C increased from 12.4 to 17.1 nm and those prepared

at 170 ^{o}C increased from 14.4 to 15.2 nm (Table 2.3 and Figure 2.13). Reducing the surfactant concentration appears to accelerate the rate of growth, but result in less uniform size and shape compared with nanoparticles prepared at a threefold higher ratio of surfactant to CpFe(benz-H) (Table 2.2).

Table 2.3 Size of Fe nanoparticles prepared in 0.25 M OAm at different temperatures.

Reaction temperature (^{o}C)	Particle diameter (nm)	Rel. Std. Dev. (%)
130	15.3 ± 1.9 (N=113)	12.4
150	17.1 ± 1.8 (N=133)	10.5
170	15.2 ± 1.9 (N=141)	12.5

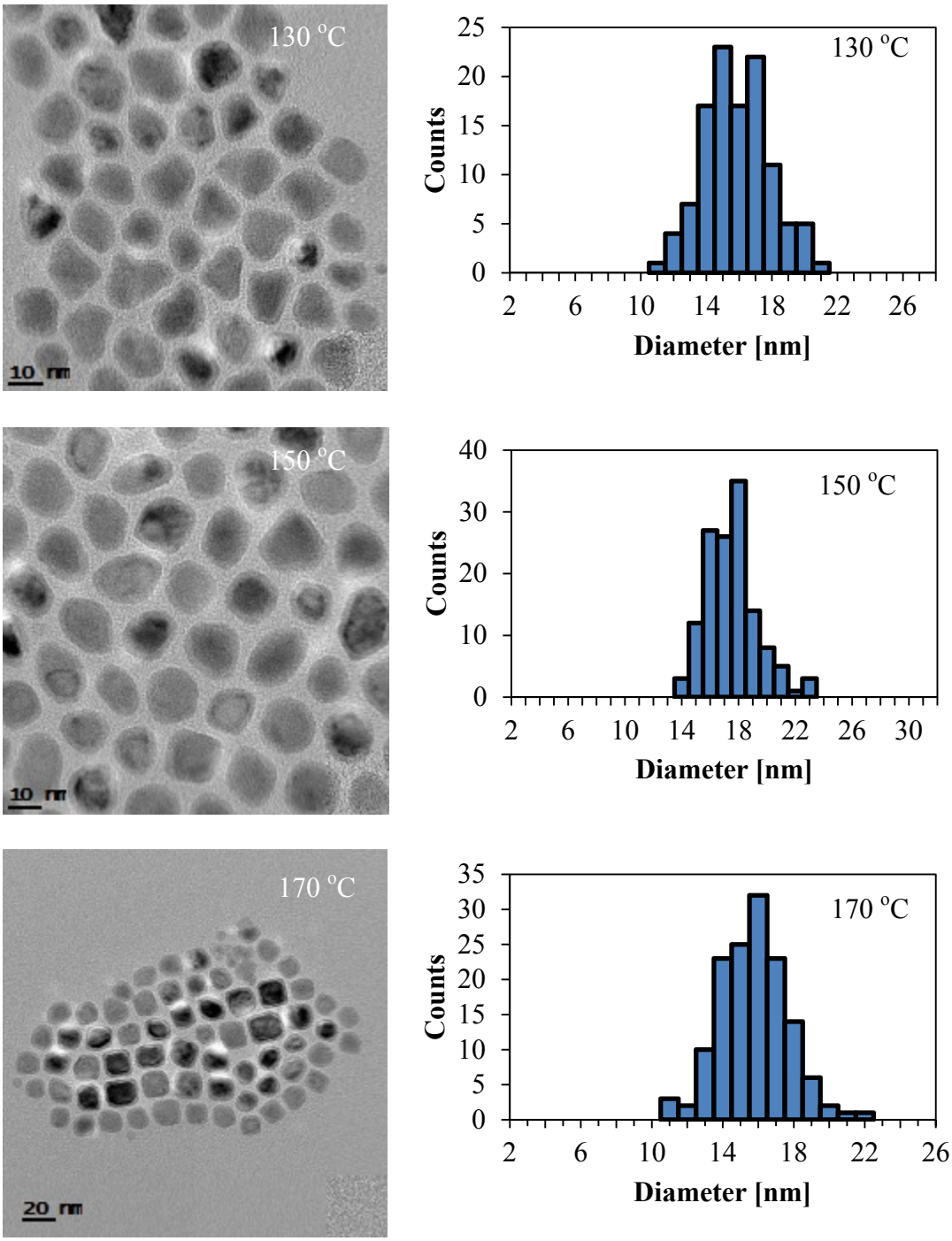

Figure 2.13 Left, TEM images of Fe nanoparticles synthesized in 0.25 M OAm/8.3 mM OAm.HCl; right, particle size analyses at different reaction temperatures (see Table 2.3 for details).

Inverse FFT analysis from HRTEM images of individual nanoparticles from samples heated at 150 ^{o}C and 170 ^{o}C resulted in *d* spacing values of 1.98 and 2.01 Å, which again confirmed the presence of a bcc-Fe core (Figure 2.14).

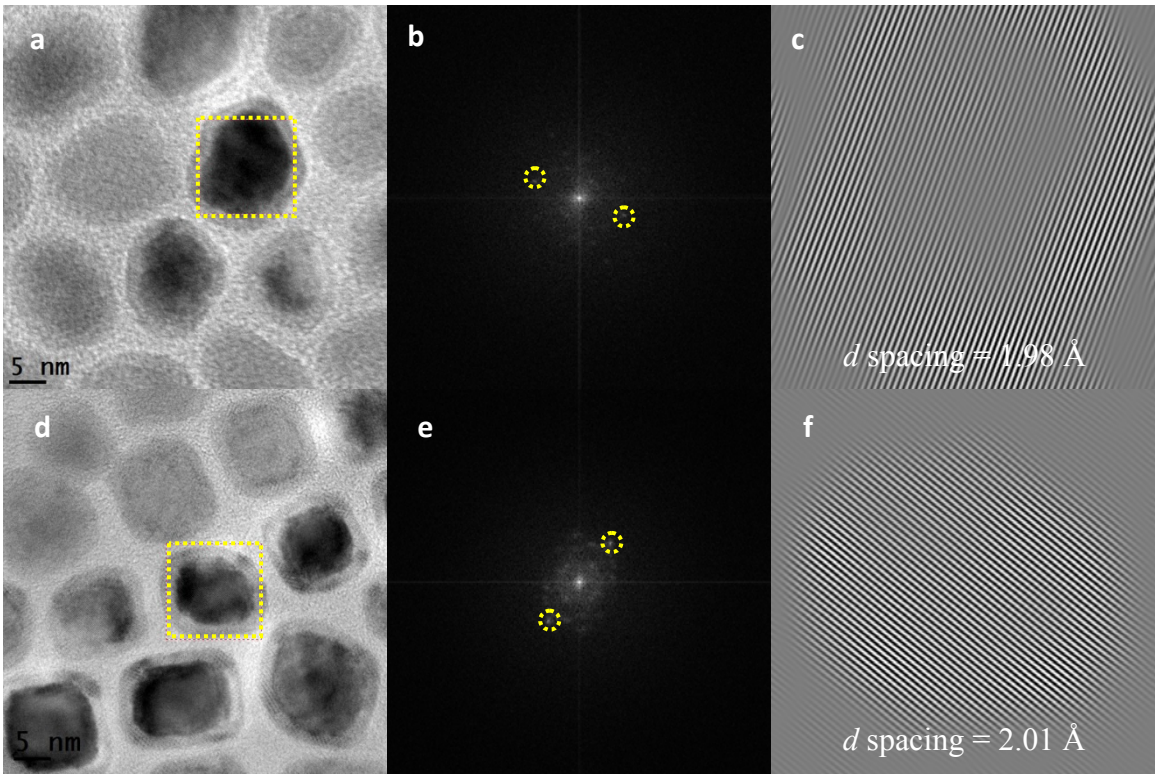

Figure 2.14 HRTEM, FFT and inverse FFT images of single nanoparticles from samples heated at 150 ^{o}C (a−c) and 170 ^{o}C (d−f).

2.3.5 Effect of Organoiron Reagent

In order to investigate whether the aromatic moiety in the organoiron sandwich complex had any effect on iron nanoparticle formation, we evaluated (π-C_5H_5)Fe^0(*p*-xylene-H) CpFe(xyl-H) as a precursor in place of CpFe(benz-H).

CpFe(xyl-H) was prepared by treating ferrocene (2.1 g) with $AlCl_3$ (3 equiv.), Al (1 equiv.) and a few drops of water in *p*-xylyne (20 mL) at relux 1.5 hours. The reaction mixture was poured over ice and the aqueous phase was separated and washed three times with hexanes. The aqueous solution was treated with KPF_6 (1.23 equiv.), which caused the precipitation of a green solid. This was filtered and dried under vacuum to produce 3.8 g of CpFe(xylene)-PF_6 salt (90% yield). The green solid was filtered and dried under vacuum, suspended in dry THF and cooled in an ice bath, then treated with $LiAlH_4$ (2.5 equiv) added in portions. After 15 min, the reaction was quenched with water and the orange/red reaction mixture was transferred to a separatory funnel, diluted with H_2O, and extracted 3 times with hexanes. The hexane fractions were dried over $NaSO_4$, filtered, and concentrated to give a red oily liquid, which was purified by vacuum distillation at 70 ^oC and 0.5 torr. The isolated yield of CpFe(xyl-H) was 1.2 g (58%)

The nanoparticle synthesis with CpFe(xyl-H) was conducted in *n*-decane (0.30 M). at 130 ^oC for 48 h, in the presence of OAm (0.90 M) and OAm.HCl (0.03 M). Although the concentration of CpFe(xyl-H) was slightly higher than the reactions with CpFe(benz-H), the ratio of precursor to surfactant was kept the same. TEM analysis showed that most nanoparticles were cubic and uniform in size, the average edge length was 13.6 ± 0.9 nm (*N*=129; Figure 2.15), just slightly larger than nanoparticles synthesized using CpFe(benz-H).

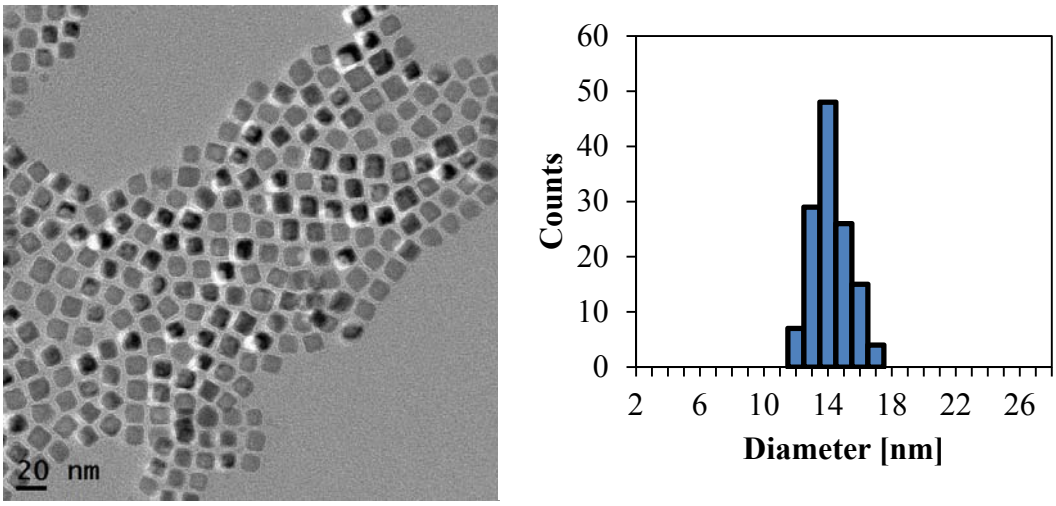

Figure 2.15 TEM image (left) and size distribution (right) of the nanoparticles from sample using CpFe (xyl-H) as a reagent.

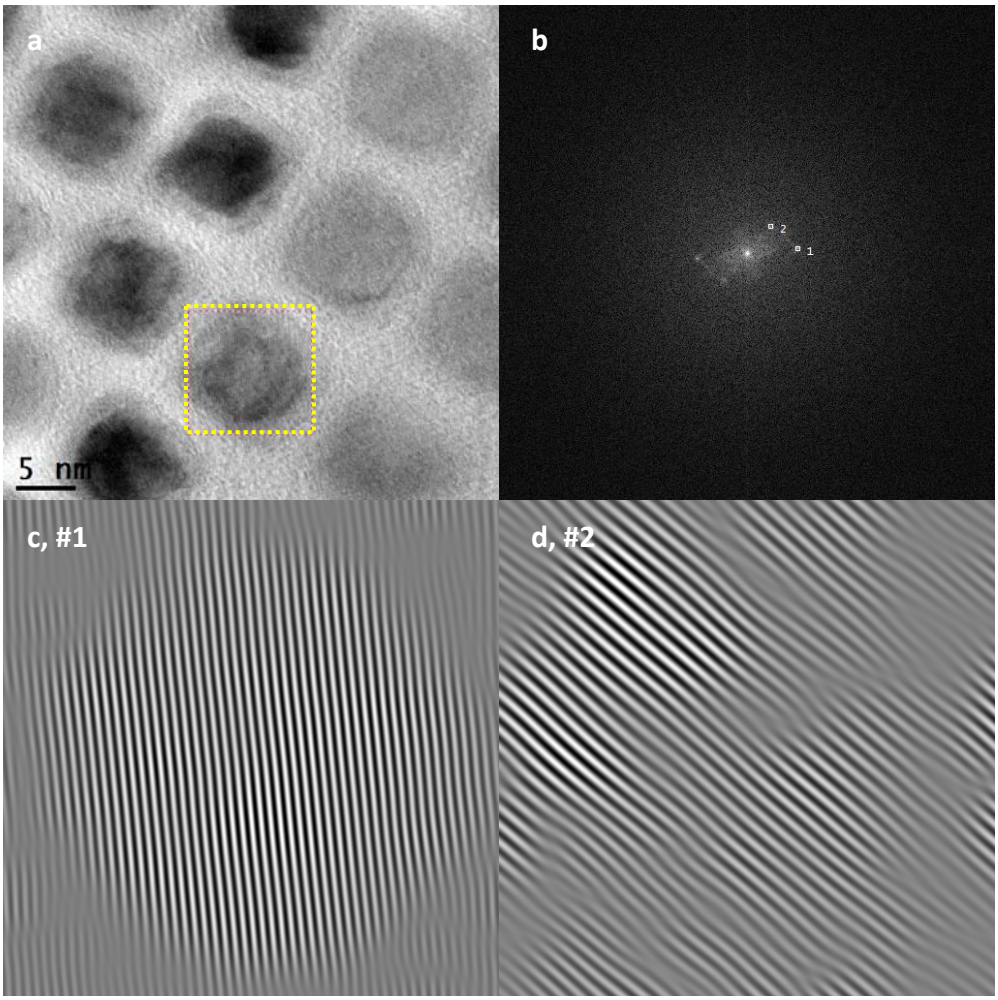

Figure 2.16 (a−d) HRTEM, FFT and inverse FFT images representing bcc-Fe and Fe_3O_4 in single nanoparticle from sample using CpFe(xyl-H) as precursor.

HRTEM analysis of the nanoparticles (Figure 2.16a) again showed the formation of core/shell structures, and FFT analysis produced two sets of reciprocal lattice peaks, with *d* spacing values of 1.99 Å (#1) and 2.85 Å (#2), corresponding to bcc-Fe and Fe_3O_4 (Figure 2.16c and 2.16d, respectively). The inverse FFT analysis of reciprocal lattice peak #1 showed the bcc-Fe lattices to coincide with the nanoparticle core, whereas that of

#2 was mainly associated with the shell structure. The measured *d* spacing values from the both lattice peaks are summarized in Table 2.4.

Table 2.4 FFT analysis of iron nanoparticles prepared from CpFe(xyl-H).

#	Measured d values (Å)	d values (Å) JCPDS #06-0696 (bcc-Fe)	hkl (%)	d spacing (Å) JCPDS #19-0629 (Fe_3O_4)	hkl (%)
1	1.99	2.03	110 (100)		
2	2.85			2.97	220 (30)

2.3.6 Conclusions

A method for the synthesis of crystalline core/shell iron/iron oxide nanocubes has been optimized. Iron nanocubes were synthesized by decomposition of a organoiron complex, CpFe(benz-H) in sealed reaction vessels, at 130−170 ^{o}C. The best conditions for obtaining uniform Fe/Fe_3O_4 core/shell nanocubes were based on *n*-decane as a solvent, in the presence of oleylamine and oleylamine.HCl at 0.75 M and 0.025 M respectively. TEM analysis confirmed the core/shell structures, and FFT analysis confirmed the presence of bcc-Fe in the core and iron oxide (Fe_3O_4 or γ-Fe_2O_3) in the shell. Reaction parameters such as temperature, surfactant concentration, counterion, and chemical structure of the organoiron reagetn were investigated. These results show that the size and the shape of the Fe nanocubes can be optimized by systematic tuning of the reaction parameters.

.

LIST OF REFERENCES

LIST OF REFERENCES

1. Callister, W. D.; Rethwisch, D. G., Materials Science and Engineering: An Introduction, 8th Edition. In *Materials Science and Engineering: An Introduction, 8th Edition*, Willey: 2010.

2. Leslie-Pelecky, D. L.; Rieke, R. D., Magnetic Properties of Nanostructured Materials. *Chemistry of Materials* **1996,** *8* (8), 1770-1783.

3. Huber, D. L., Synthesis, Properties, and Applications of Iron Nanoparticles. *Small* **2005,** *1* (5), 482-501.

4. (a) Lacroix, L.-M.; Frey Huls, N.; Ho, D.; Sun, X.; Cheng, K.; Sun, S., Stable Single-Crystalline Body Centered Cubic Fe Nanoparticles. *Nano Letters* **2011,** *11* (4), 1641-1645; (b) Cheong, S.; Ferguson, P.; Feindel, K. W.; Hermans, I. F.; Callaghan, P. T.; Meyer, C.; Slocombe, A.; Su, C.-H.; Cheng, F.-Y.; Yeh, C.-S.; Ingham, B.; Toney, M. F.; Tilley, R. D., Simple Synthesis and Functionalization of Iron Nanoparticles for Magnetic Resonance Imaging. *Angewandte Chemie International Edition* **2011,** *50* (18), 4206-4209.

5. Gordon, R. T.; Hines, J. R.; Gordon, D., Intracellular hyperthermia a biophysical approach to cancer treatment via intracellular temperature and biophysical alterations. *Medical Hypotheses 5* (1), 83-102.

6. Lu, A.-H.; Salabas, E. L.; Schüth, F., Magnetic Nanoparticles: Synthesis, Protection, Functionalization, and Application.

7. (a) Peng, S.; Wang, C.; Xie, J.; Sun, S., Synthesis and Stabilization of Monodisperse Fe Nanoparticles. *Journal of the American Chemical Society* **2006,** *128* (33), 10676-10677; (b) Cabot, A.; Puntes, V. F.; Shevchenko, E.; Yin, Y.; Balcells, L.; Marcus, M. A.; Hughes, S. M.; Alivisatos, A. P., Vacancy Coalescence during Oxidation of Iron Nanoparticles. *Journal of the American Chemical Society* **2007,** *129* (34), 10358-10360.

8. Suslick, K. S.; Fang, M.; Hyeon, T., Sonochemical Synthesis of Iron Colloids. *Journal of the American Chemical Society* **1996,** *118* (47), 11960-11961.

9. Park, S.-J.; Kim, S.; Lee, S.; Khim, Z. G.; Char, K.; Hyeon, T., Synthesis and Magnetic Studies of Uniform Iron Nanorods and Nanospheres. *Journal of the American Chemical Society* **2000,** *122* (35), 8581-8582.

10. Dumestre, F.; Chaudret, B.; Amiens, C.; Renaud, P.; Fejes, P., Superlattices of Iron Nanocubes Synthesized from Fe[N(SiMe3)2]2. *Science* **2004,** *303* (5659), 821-823.

11. Shavel, A.; Rodríguez-González, B.; Spasova, M.; Farle, M.; Liz-Marzán, L. M., Synthesis and Characterization of Iron/Iron Oxide Core/Shell Nanocubes. *Advanced Functional Materials* **2007,** *17* (18), 3870-3876.

12. Lacroix, L.-M.; Lachaize, S. b.; Falqui, A.; Respaud, M.; Chaudret, B., Iron Nanoparticle Growth in Organic Superstructures. *Journal of the American Chemical Society* **2008,** *131* (2), 549-557.

13. Green, M. L. H.; Pratt, L.; Wilkinson, G., 206. Spectroscopic studies of some organoiron complexes. *Journal of the Chemical Society* **1960,** *0* (0), 989-997.